

Geochemistry, Geophysics, Geosystems



RESEARCH ARTICLE

10.1029/2019GC008297

Special Section:

Polar region geosystems

Key Points:

- The Sparsely Magmatic Zone (Gakkel Ridge) geochemistry and topography represent the low extreme for global seafloor spreading ridges
- The first age dating of a Gakkel Ridge rock sample shows that seafloor spreading is active along the eastern part of the ridge
- The study contributes to our global understanding of ultraslow spreading mid-ocean ridges

Supporting Information:

- Supporting Information S1

Correspondence to:

W. Jokat,
wilfried.jokat@awi.de

Citation:

Jokat, W., O'Connor, J., Hauff, F., Koppers, A. A. P., & Miggins, D. P. (2019). Ultraslow spreading and volcanism at the eastern end of Gakkel Ridge, Arctic Ocean. *Geochemistry, Geophysics, Geosystems*, 20. <https://doi.org/10.1029/2019GC008297>

Received 26 FEB 2019

Accepted 5 NOV 2019

Accepted article online 3 SEP 2019

©2019. The Authors.

This is an open access article under the terms of the Creative Commons Attribution License, which permits use, distribution and reproduction in any medium, provided the original work is properly cited.

Ultraslow Spreading and Volcanism at the Eastern End of Gakkel Ridge, Arctic Ocean

Wilfried Jokat^{1,2} , John O'Connor^{1,3,4} , Folkmar Hauff⁵ , Anthony A.P. Koppers⁶ , and Dan P. Miggins⁶

¹Alfred Wegener Institute Helmholtz Centre for Polar and Marine Research, Bremerhaven, Germany, ²Faculty of Geosciences, University of Bremen, Bremen, Germany, ³GeoZentrum Nordbayern, University Erlangen-Nürnberg, Erlangen, Germany, ⁴Faculty of Science, VU University Amsterdam, Amsterdam, Netherlands, ⁵GEOMAR Helmholtz Centre for Ocean Research Kiel, Kiel, Germany, ⁶College of Earth, Ocean, and Atmospheric Sciences, Oregon State University, Corvallis, OR, USA

ABSTRACT Ultraslow spreading ridges are poorly understood plate boundaries consisting of magmatic and amagmatic segments that expose mostly mantle peridotite and only traces of basalt and gabbro. The slowest part of the global spreading system is represented by the eastern Gakkel Ridge in the Central Arctic Ocean, where crustal accretion is characterized by extreme focusing of melt to discrete magmatic centers. Close to its eastern tip lies the unusual 5,310-m-deep Gakkel Ridge Deep (GRD) with limited sediment infill, which is in strong contrast to the broader sediment-filled rift valleys to the east and west. Here, we report an ⁴⁰Ar/³⁹Ar age of 3.65 ± 0.01 Ma for a pillow basalt from a seamount located on the rim the GRD, confirming ultraslow spreading rates of ~ 7 mm/year close to the Laptev Sea as suggested from aeromagnetic data. Its geochemistry points to an alkaline lava, attributed to partial melting of a source that underwent prior geochemical enrichment. We note that the GRD extracts compositionally similar melts as the sparsely magmatic zone further west but at much slower spreading velocities of only $\sim 6\text{--}7$ mm/year, indicating the widespread occurrence of similarly fertile mantle in the High Arctic. This enriched source differs from subcontinental lithospheric mantle that influences magmatism along the Western Volcanic Zone (Goldstein et al., 2008, <https://doi.org/10.1038/nature06919>) and is similar to metasomatized mantle, shown to influence melt genesis along the Eastern Volcanic Zone.

1. Introduction

The Gakkel Ridge extending for 1,800 km under the Arctic ice is the slowest spreading ridge on Earth with estimated full spreading rates varying from ~ 13 mm/year in the west to only ~ 6 mm/year in the east (Brozena et al., 2003; Karasik, 1968; Vogt et al., 1979). There is growing evidence that the Gakkel Ridge expresses unique modes of crustal accretion and tectonic extension (Cochran, 2008; Dick et al., 2003; Jokat et al., 2003; Jokat & Schmidt-Aursch, 2007; Michael et al., 2003; Schlindwein & Schmidt, 2016; Sohn et al., 2008). Moreover, because it contains no significant transform offsets that can act as boundaries to mantle flow and composition, it is an ideal place to study mantle source heterogeneity and melting dynamics at ultraslow spreading rates and the processes contributing to the composition of the Arctic mantle (Dick et al., 2003; Goldstein et al., 2008; Michael et al., 2003; Schlindwein & Schmidt, 2016).

Based on the first systematic geophysical/petrological study along most of the Gakkel Ridge between 7°W and 85°E (Jokat et al., 2003; Michael et al., 2003) the Gakkel Ridge was divided into three tectonic segments, composed of robust Western (WVZ) and Eastern (EVZ) Volcanic Zones separated by a “Sparsely Magmatic Zone” (SMZ) (Figure 1).

The WVZ has mid-Atlantic ridge-type morphology with a 15-km-wide rift, axial volcanic ridges, volcanoes scattered on the valley floor, and rift valley walls consisting of high-angle faults (Cochran, 2008). The number and size of volcanic features are, however, greatly reduced compared to those of the slow spreading Mid-Atlantic Ridge (e.g., Cochran, 2008; Jokat et al., 2003). Basalts were recovered by dredging almost exclusively in this segment (Figure 1d), carrying a pronounced magnetic anomaly of up to 500 nT.

Further to the east, the SMZ and EVZ display a very different mode of crustal accretion. The transition from the WVZ to the SMZ at 03°30'E is abrupt: Water depths drop from 4,000 to 5,200 m, the magnetic field decreases to low values around 10 nT, and in this 300-km-long segment less than 20% of the rift valley is

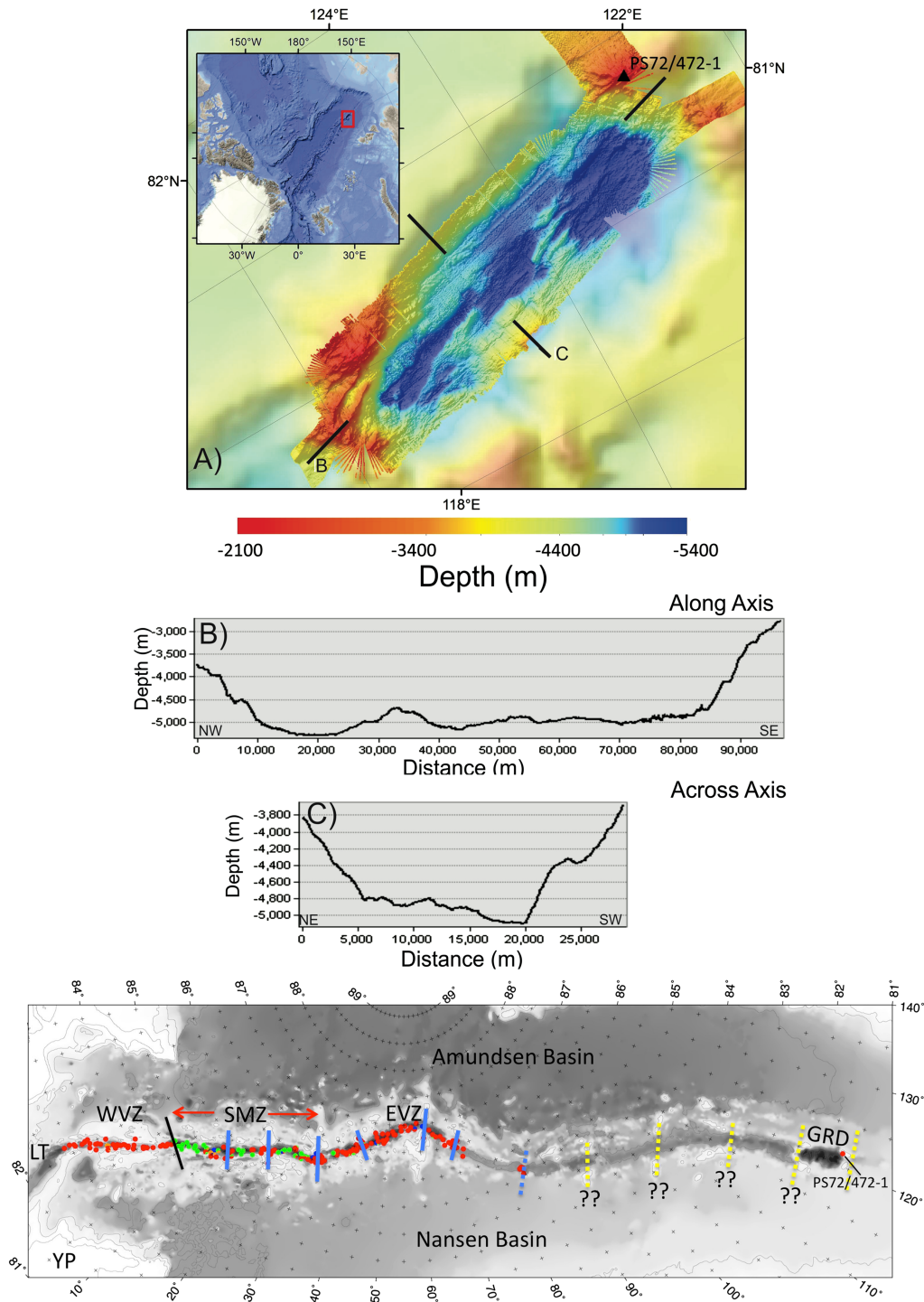


Figure 1. (a–c) Inset shows the bathymetry of the Eurasian Basin in the Arctic Ocean (IBCAO grid v3, 500-m grid resolution) (Jakobsson et al., 2012). The red box indicates our research area. (a) The swath bathymetry acquired during two RV *Polarstern* cruises. Rock sample PS72/472-1 was recovered from Shaykin Seamount during the RV *Polarstern* cruise ARK-XXIII/3. Dredge track from 81°12.76'N, 121°25.87'E, 3,257-m water depth to 81°12.15'N, 121°31.26'E, 2,474-m water depth. See Jokát (2009) for further details. The black lines indicate the location of the along- and across-axis depth profiles shown in (b) and (c), respectively. (d) Bathymetry of the Gakkel Ridge and the adjacent deep sea plains (Jakobsson et al., 2012). Sample locations are marked according to Michael et al. (2003). Red = basalt; green = peridotite; orange = gabbro; blue = others. The colored lines mark different tectonic elements: black line = eastern termination of the WVZ; blue lines = volcanic basement ridges (six) perpendicular to the rift valley, which subdivide the three general segments; dashed blue line = location of recent volcanism (Müller & Jokát, 2000; Sohn et al., 2008), dashed yellow lines = suggested location of transverse volcanic basement ridges caused by focused magmatism but almost completely covered by sediments. Abbreviations: EVZ = Eastern Volcanic Zone; GRD = Gakkel Ridge Deep; LT = Lena Trough; SMZ = Sparsely Magmatic Zone; WVZ = Western Volcanic Zone; YP = Yermak Plateau.

covered by basalts (Figure 1d; Michael et al., 2003). In contrast to the WVZ segment, the SMZ and EVZ segments are characterized by a total of six magmatic basement ridges with a spacing of 100 km. These ridges carry a strong magnetic signal of up to 500 nT, which declines to low values close to 0 nT between them (Jokat & Schmidt-Aursch, 2007) and correlates with dredging results. Within the SMZ, basalts were mostly dredged in the vicinity of the magmatic ridges, while peridotites were recovered in between. In the EVZ basalts dominate again the seafloor between the basement ridges. These data were interpreted as evidence for extreme focusing of melt into discrete magmatic centers, which might be related to local diapirism resulting from localized melting of inhomogeneities embedded in a heterogeneous (veined?) mantle (Jokat et al., 2003; Michael et al., 2003).

It is still unknown whether this pattern of ridge segmentation continues at even slower spreading rates of ~6 mm/year along the remaining portion of the Gakkel Ridge toward the Laptev Sea, since the rift valley east of 70°E is filled by several-kilometer-thick sediments (Jokat & Micksch, 2004; Nikishin et al., 2017; Sekretov, 2002). East of 85°E, only a few high standing flanks of the rift valley are accessible to basement sampling. A notable exception occurs between 81°10'N and 82°N latitude along 120°E longitude (Figure 1). Here, on the easternmost part of the Gakkel Ridge, bathymetric data reveal a deep depression (maximum 5,310 m) almost devoid of sediments and thus referred to as the Gakkel Ridge Deep (GRD) (Figure 1; Nikishin et al., 2017). Seismic reflection data (Nikishin et al., 2017; Piskarev & Elkina, 2017) confirm the near absence of sediment in the GRD. Despite the lack of basement exposure, no information about lithology, crustal thickness, and age of the easternmost Gakkel Ridge rift valley is so far available. Recent swath mapping shows that the GRD is roughly 97 km long, 30 km wide, with a basin depth that is 1,800–2,000 m deeper than the surrounding flanks, which are composed of several volcanic peaks and mounds (Figures 1a–1c). The central part of the GRD reveals rift-parallel ridges up to 0.5–1 km high, similar to other mid-ocean rift valleys (Figures 1a–1c). Overall, a 10-km-wide, tectonically active, divergent plate boundary is evident for the central GRD.

Here we report high-precision $^{40}\text{Ar}/^{39}\text{Ar}$ age, geochemical, and Sr-Nd-Pb isotopic data for a highly plagioclase porphyritic pillow lava (PS72/472-1) dredged from the northeast rim of the GRD at 81°12.76'N/121°25.87'E (Jokat, 2009) (Figure 1). We use these data, in combination with geophysical information (Jokat & Micksch, 2004; Nikishin et al., 2017; Piskarev & Elkina, 2017), to investigate the age/origin of the GRD and its implications for understanding mantle melting processes at extremely low spreading rates and if magmatism is still focused at the eastern end of the Gakkel Ridge.

2. Methods

2.1. Geochemistry

Bulk rock powder of the GRD sample PS72/472-1 was prepared by established standard procedures at GEOMAR using a jaw crusher, agate mortar, and agate swing mill (see also Rohde et al., 2013, for technical details). Due to the highly plagioclase porphyritic nature of the lava, about 50 g of rock chips was milled to assure homogeneity. For Sr-Nd-Pb isotope analysis 0.5- to 1-mm groundmass rock chips were picked under a binocular microscope. No fresh glass is present along the thin (<1 mm) palagonitized glassy margin of the pillow. Major element and some trace element data were obtained by X-ray fluorescence on fused beads with a Philipps X'Unique spectrometer at GEOMAR. H₂O and CO₂ were determined with a Rosemount infrared photometer. A full set of trace element concentrations were obtained by solution inductively coupled plasma mass spectrometry on an Agilent 7500cs instrument at the Institute of Geosciences at Kiel University following the methods of Garbe-Schönberg (1993). Sr-Nd-Pb isotope analyses were carried out on mildly leached groundmass chips (2 M HCl at 70 °C for 1 hr) by thermal ionization mass spectrometry as outlined in Hoernle et al. (2011). A second Sr isotope analysis used strongly leached powders (6 M HCl at 150 °C for 12 hr) to remove the effects of seawater alteration more efficiently. Analytical data along with standard measurements are provided in Table 1.

Correction of bulk rock analyses for plagioclase accumulation used average ~An89 compositions of samples HB12B-1 and HB12B-2 at https://serc.carleton.edu/NAGTWorkshops/petrology/teaching_examples/24648.html. For each correction step, percentages are calculated for the main plagioclase constituents (SiO₂, Al₂O₃,

Table 1
Major Element, Trace Element and Radiogenic Sr-Nd-Pb Isotope Data of Sample PS72/472-1 Along With Reference Materials Analyzed

| | Method | Unit | Sample ID | | Standards | | |
|--------------------------------|--------|------|------------|-------|-----------|--------|-------|
| | | | PS72/472-1 | JA-2 | JB-2 | JB-3 | JR-1 |
| SiO ₂ | XRF | wt% | 49.24 | 56.24 | 53.03 | 50.8 | 74.92 |
| TiO ₂ | XRF | wt% | 1.69 | 0.67 | 1.17 | 1.41 | 0.11 |
| Al ₂ O ₃ | XRF | wt% | 20.12 | 15.45 | 14.77 | 17.21 | 12.84 |
| Fe ₂ O ₃ | XRF | wt% | 8.21 | 6.38 | 14.45 | 11.98 | 0.85 |
| MnO | XRF | wt% | 0.12 | 0.11 | 0.21 | 0.17 | 0.1 |
| MgO | XRF | wt% | 2.75 | 8.04 | 4.71 | 5.2 | 0.14 |
| CaO | XRF | wt% | 12.03 | 6.26 | 9.89 | 9.75 | 0.7 |
| Na ₂ O | XRF | wt% | 3.82 | 2.98 | 2.03 | 2.76 | 4.11 |
| K ₂ O | XRF | wt% | 0.69 | 1.75 | 0.41 | 0.77 | 4.46 |
| P ₂ O ₅ | XRF | wt% | 0.32 | 0.15 | 0.1 | 0.29 | 0.03 |
| Co | XRF | ppm | 28 | 30 | 47 | 41 | 5 |
| Cr | XRF | ppm | 199 | 451 | 29 | 68 | b.d.l |
| Ni | XRF | ppm | 22 | 112 | 28 | 30 | b.d.l |
| V | XRF | ppm | 240 | 126 | 558 | 385 | b.d.l |
| Zn | XRF | ppm | 58 | 64 | 109 | 99 | 30 |
| Nb | XRF | ppm | 17 | 9 | b.d.l | b.d.l | 14 |
| Ga | XRF | ppm | 21 | 21 | 18 | 26 | 19 |
| Rb | XRF | ppm | 11 | 76 | 10 | 19 | 269 |
| Ba | XRF | ppm | 95 | 314 | 235 | 248 | 44 |
| Sr | XRF | ppm | 379 | 240 | 178 | 403 | 28 |
| Y | XRF | ppm | 24 | 3 | 21 | 22 | 11 |
| Zr | XRF | ppm | 154 | 88 | 42 | 83 | 82 |
| Sum | XRF | wt% | 99.15 | 98.21 | 100.94 | 100.51 | 98.33 |
| H ₂ O | XRF | wt% | 0.84 | n.a. | n.a. | n.a. | n.a. |
| CO ₂ | XRF | wt% | 0.02 | n.a. | n.a. | n.a. | n.a. |
| Total | XRF | wt% | 100.01 | | | | |
| | | | | BIR-1 | BHVO-2 | BCR-2 | |
| Li | ICPMS | ppm | 6.10 | 3.19 | 4.52 | 8.88 | |
| Sc | ICPMS | ppm | 36.3 | 44.3 | 32.7 | 34.9 | |
| V | ICPMS | ppm | 250 | 311 | 322 | 420 | |
| Cr | ICPMS | ppm | 210 | 374 | 293 | 19 | |
| Co | ICPMS | ppm | 23.4 | 51.50 | 44.96 | 37.72 | |
| Ni | ICPMS | ppm | 39.2 | 166 | 119 | 12.1 | |
| Cu | ICPMS | ppm | 56.4 | 125 | 134 | 20.3 | |
| Zn | ICPMS | ppm | 57.6 | 70.2 | 104.15 | 133 | |
| Ga | ICPMS | ppm | 19.2 | 16.0 | 22.40 | 23.4 | |
| Rb | ICPMS | ppm | 8.88 | 0.23 | 9.32 | 48.5 | |
| Sr | ICPMS | ppm | 376 | 107 | 387 | 339 | |
| Y | ICPMS | ppm | 28.0 | 15.8 | 25.66 | 35.8 | |
| Zr | ICPMS | ppm | 153 | 14.7 | 170 | 189 | |
| Nb | ICPMS | ppm | 16.2 | 0.52 | 17.7 | 12.0 | |
| Cs | ICPMS | ppm | 0.167 | 0.006 | 0.11 | 1.15 | |
| Ba | ICPMS | ppm | 116 | 6.33 | 132 | 664 | |
| La | ICPMS | ppm | 12.0 | 0.585 | 15.4 | 25.2 | |
| Ce | ICPMS | ppm | 27.3 | 1.86 | 38.3 | 52.9 | |
| Pr | ICPMS | ppm | 3.76 | 0.363 | 5.39 | 6.83 | |
| Nd | ICPMS | ppm | 16.8 | 2.33 | 24.4 | 28.9 | |
| Sm | ICPMS | ppm | 4.42 | 1.080 | 6.13 | 6.59 | |
| Eu | ICPMS | ppm | 1.58 | 0.513 | 2.07 | 1.95 | |
| Gd | ICPMS | ppm | 4.95 | 1.74 | 6.21 | 6.75 | |
| Tb | ICPMS | ppm | 0.826 | 0.349 | 0.935 | 1.05 | |
| Dy | ICPMS | ppm | 5.21 | 2.52 | 5.36 | 6.36 | |
| Ho | ICPMS | ppm | 1.06 | 0.562 | 0.983 | 1.28 | |
| Er | ICPMS | ppm | 2.89 | 1.61 | 2.44 | 3.48 | |
| Tm | ICPMS | ppm | 0.424 | 0.244 | 0.328 | 0.519 | |
| Yb | ICPMS | ppm | 2.74 | 1.62 | 2.00 | 3.36 | |

(Continues)

Table 1
(continued)

| | Method | Unit | Sample ID | | Standards | | |
|----|--------|------|------------|-------|-----------|-------|------|
| | | | PS72/472-1 | JA-2 | JB-2 | JB-3 | JR-1 |
| Lu | ICPMS | ppm | 0.410 | 0.244 | 0.280 | 0.500 | |
| Hf | ICPMS | ppm | 3.35 | 0.551 | 4.33 | 4.71 | |
| Ta | ICPMS | ppm | 0.994 | 0.040 | 1.10 | 0.727 | |
| Pb | ICPMS | ppm | 1.17 | 2.98 | 1.67 | 10.7 | |
| Th | ICPMS | ppm | 1.05 | 0.029 | 1.19 | 5.67 | |
| U | ICPMS | ppm | 0.452 | 0.012 | 0.409 | 1.61 | |

| | Method | Sample ID | | Standards | | |
|---|--------|------------|-----------------|-----------|----|----------|
| | | PS72-472-1 | NBS981 | 2SD | N | 2SE |
| ²⁰⁶ Pb/ ²⁰⁴ Pb | TIMS | 18.3196 | 16.9413 | 0.0019 | 30 | 0.0018 |
| ²⁰⁷ Pb/ ²⁰⁴ Pb | TIMS | 15.5015 | 15.4995 | 0.0019 | 30 | 0.0016 |
| ²⁰⁸ Pb/ ²⁰⁴ Pb | TIMS | 37.9764 | 36.7241 | 0.0048 | 30 | 0.0040 |
| ²⁰⁷ Pb/ ²⁰⁶ Pb | TIMS | 0.84617 | 0.91489 | 0.00004 | 30 | 0.00001 |
| ²⁰⁸ Pb/ ²⁰⁶ Pb | TIMS | 2.07299 | 2.16772 | 0.00007 | 30 | 0.00005 |
| | | | NBS987 | | | |
| ⁸⁷ Sr/ ⁸⁶ Sr | TIMS | 0.702942 | 0.710250 | 0.000012 | 12 | 0.000005 |
| ⁸⁷ Sr/ ⁸⁶ Sr ^a | | 0.702939 | | | | 0.000005 |
| | | | La Jolla | | | |
| ¹⁴³ Nd/ ¹⁴⁴ Nd | TIMS | 0.513044 | 0.511850 | 0.000008 | 12 | 0.000005 |
| Epsilon Nd | | 7.93 | | | | |

^a6 M HCl leached powder at 150 °C for 12 hr, All others are 2 M HCl leached chips at 70 °C for 1 hr for Sr-Nd-Pb isotope analysis.

CaO, Na₂O, and K₂O), subtracted from the measured bulk rock composition, and then the residual melt normalized to the initially measured total of 99.85 wt% to obtain a simulation of the erupted melt composition.

2.2. Geochronology—Sample Preparation

The groundmass samples were prepared following the methods of Koppers et al. (2012). The 200- to 180- μ m samples measured at Oregon State were cleaned in a series of hour-long acid baths, progressing from 1 N HCl to 6 N HCl to 1 N HNO₃ to 3 N HNO₃, followed by a final Milli-Q water bath. Each separate was picked by hand under a binocular microscope to ensure the removal of alteration and to confirm the purity of the separate.

Groundmass samples were irradiated for 6 hr in the CLICIT (Cadmium-Lined In-Core Irradiation Tube) position at the Oregon State University TRIGA[®] reactor. Incremental heating experiments were conducted for each sample. Irradiated samples were loaded into copper planchettes for analysis using a Thermo Scientific ARGUS-VI multicollector mass spectrometer at the Oregon State University Argon Geochronology Laboratory following the procedure described in Konrad et al. (2018). All ages are calculated relative to Fish Canyon Tuff sanidine with an age of 28.201 Ma (Kuiper et al., 2008) and using the decay constants after Min et al. (2000).

The correction factors for neutron interference reactions at the TRIGA[®] are $(2.64 \pm 0.02) \times 10^{-4}$ for (³⁶Ar/³⁷Ar)_{Ca}, $(6.73 \pm 0.04) \times 10^{-4}$ for (³⁹Ar/³⁷Ar)_{Ca}, $(1.21 \pm 0.003) \times 10^{-2}$ for (³⁸Ar/³⁹Ar)_K, and $(8.6 \pm 0.7) \times 10^{-4}$ for (⁴⁰Ar/³⁹Ar)_K. Ages were calculated using the ArArCALC v2.7.052 software of Koppers (2002), with errors including uncertainties on the blank corrections, irradiation constants, J-curve, collector calibrations, mass fractionation, and the decay of ³⁷Ar and ³⁹Ar.

2.3. Geochronology—Data Quality

⁴⁰Ar/³⁹Ar step-heating experiments were assessed based on the following criteria: An acceptable age plateau (1) includes at least 50% of the gas released, (2) has a mean square weighted deviation of approximately 1.0

and within the statistically allowed upper limit, (3) shows an inverse isochron with a $^{40}\text{Ar}/^{36}\text{Ar}$ intercept of about $295.5 \pm 2\sigma$, and (4) has concordant plateau, isochron, and total fusion ages. See more details in the supporting information.

3. Results and Preliminary Inferences

3.1. Major Elements

Bulk chemistry of PS72/471-1 reveals a fairly fresh ($\text{H}_2\text{O} = 0.84 \text{ wt\%}$, $\text{CO}_2 = 0.02 \text{ wt\%}$) but differentiated lava ($\text{MgO} = 2.75 \text{ wt\%}$; $\text{Mg\#} = \sim 40$; $100 \times \text{Mg}/(\text{Mg} + \text{Fe})$). Lavas with similarly low Mg# are rare along the Gakkel Ridge but occur subordinate in the EVZ and E-SMZ ($\text{Mg\#} \sim 39$ to 49 at $\text{MgO} = 4.5$ to 5.9 wt\%). The total alkali-silica diagram (Le Maitre et al., 2005) (Figure 2) reveals an alkali basaltic composition that occurs only occasionally throughout the Gakkel Ridge (glass compilation of Gale et al., 2013). Correction for plagioclase accumulation (see below), however, shifts the simulated melt into the trachy-basalt field (20–30% correction) and well into the basaltic trachy-andesite field (40% correction). Such high alkaline melts and differentiates thereof are unknown from the Gakkel Ridge. Major and minor element variations versus MgO show that Al_2O_3 , CaO, FeO, TiO_2 , and P_2O_5 of the bulk GRD sample (Figure 3) has the least MgO concentration of all Gakkel glasses and plots away from the correlations defined by Gakkel Ridge glasses. Al and Ca are too high for the low Mg (Figures 3a and 3b), suggesting significant plagioclase (a Na-Ca-Al-silicate) surplus that is likely caused by accumulation during eruption of this high-viscosity lava as testified by the several meter-sized pillow samples (Jokat, 2009). Incorporation of plagioclase xenocrysts from conduit/magma chamber walls may have further contributed to the plagioclase excess. Plagioclase correction shows that 30% subtraction lowers Al_2O_3 to $\sim 13.6 \text{ wt\%}$ at 3.9 wt\% MgO and aligns the simulated GRD melt to differentiated glasses from the EVZ and E-SMZ (Figure 3a). Similarly, a $\sim 35\%$ An89 correction lowers CaO to $\sim 8.8 \text{ wt\%}$ at 4.2 wt\% MgO in line with the aforementioned EVZ and E-SMZ glasses (Figure 3b). The FeO and TiO_2 trends of these EVZ and E-SMZ glasses intersect the 40% An89 correction (Figures 3c and 3d), while 30% to 40% match P_2O_5 (Figure 3h). For Na_2O (Figure 3e) and K_2O (Figure 3f) 30–40% An89 correction, as inferred from Al, Ca, Fe, Ti, and P, leads to compositions in the simulated melts that lie above the group of differentiated EVZ and E-SMZ glasses. These discrepancies may either reflect uncertainties in the plagioclase composition of PS72/471-1 or indicate enrichment of Na_2O and K_2O in the erupted GRD melt compared to evolved EVZ and E-SMZ glasses. If the projected high Na_2O contents are real, then Na_8 (Na_2O at $\text{MgO} = 8 \text{ wt\%}$) would lie above the common Na_8 range of the Gakkel Ridge (2.8–3.6 wt% Na_2O) and indicate low degrees of mantle melting (Klein & Langmuir, 1987) formed the GRD melt. Confirmed insights on Na_8 in the erupted melt of PS72/471-1, however, require availability of fresh glass, which is not the case. Elevated K_2O (0.65–0.95 wt%) is found in few lavas from the WVZ and both SMZ segments. Notably, the latter are more mafic ($\text{MgO} = 6.6$ to 7.6 wt\%) but have similarly elevated $\text{K}_2\text{O}/\text{TiO}_2$ (0.46–0.58) to the GRD sample ($\text{K}_2\text{O}/\text{TiO}_2 = 0.41$). In summary 30% to 40% An89 correction simulates the erupted melt of PS72/471-1 to 3.9–4.6 wt% MgO and align Al, Ca, Fe, Ti, and P to compositions displayed by similarly differentiated EVZ and E-SMZ melts. Elevated Na_2O and K_2O contents in the simulated PS72/471-1 melt at 30–40% An89 correction are, however, higher than found in any other lava from the Gakkel Ridge but require confirmation by glass analysis of either chilled margins (not found) or melt inclusions.

3.2. Trace Elements

The incompatible trace element pattern of PS72/472-1 (Figure 4a) displays enrichment of the highly incompatible elements (Rb, Ba, Th, U, Nb, and Ta) over the moderately incompatible elements (Ce through Eu) and the least incompatible elements (Gd through Lu). The pattern runs subparallel to reference enriched mid-ocean ridge basalt (E-MORB; Sun & McDonough, 1989). Notably, depletions occur for Cs and Pb, which are typical of oceanic basalts (ocean island basalt [OIB], E-MORB, and normal mid-ocean ridge basalt [N-MORB]). Also, the depletion in Th is common in the vast majority of Gakkel lavas and reference E-MORB. The Sr peak and absence of an Eu depletion is in concert with the supposed plagioclase accumulation/excess. Finally, the absence of Cs, Rb, Ba, and U peaks suggests that seawater alteration is insignificant in this rock and that these fluid-mobile elements can be used to derive petrological information. PS72/472-1 defines the upper limit of highly to moderately incompatible elements throughout the Gakkel Ridge but falls well within the range of Gakkel Ridge glasses along the least incompatible element spectrum. As expected, the rare earth element (REE) pattern of PS72/472-1 (Figure 4b)

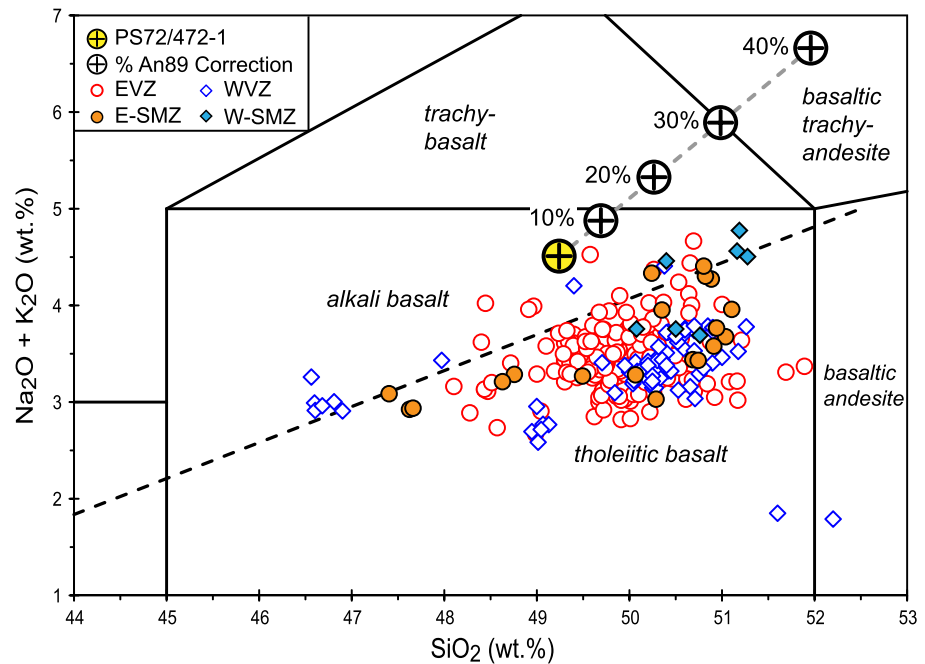


Figure 2. The total alkali versus silica diagram after Le Maitre et al. (2005) shows the bulk chemistry of PS72/471-1 lies above the alkalic-tholeiitic division line of MacDonald and Katsura (1964) plotting in the field of alkali basalts. Since PS72/471-1 is a highly plagioclase phyric lava, open circles with crosses display the composition of the erupted melt after correction for 10%, 20%, 30%, and 40% plagioclase (An89) accumulation. See text for details. For comparison, published data of volcanic glasses (compilation of Gale et al., 2013) and melt inclusions (Shaw et al., 2010; Wanless et al., 2014) from all Gakkel ridge segments are also shown. The majority of Gakkel melts are tholeiitic, while alkaline melts are infrequent but occur in each segment. See Figure 1 for the definitions of the abbreviations.

shows enrichment of the light REE (LREE) over the heavy REE (HREE) running subparallel to reference E-MORB. Only a few Gakkel Ridge patterns (10 out of 201) are also LREE enriched, but their LREE falls below PS72/472-1. They all testify to derivation from incompatible element-enriched liquids.

Ratios of incompatible elements with similar incompatibility such as Ba/Nb, Nb/La, and Zr/Hf visualize differences in source enrichment. Along-axis variations show that Ba/Nb of PS72/472-1 (Figure 5a) overlaps with EVZ west of 40°E and some E-SMZ lavas but is lower than WVZ, W-SMZ, and many E-SMZ lavas. Markedly, Ba/Nb is slightly higher than the restricted Ba/Nb of lavas and melt inclusions at 85°E, the nearest volcanic basement sampling in relation to the GRD. Nb/La (Figure 5b) of PS72/472-1 is similar to a significant number of lavas between 55°E and 10°E (EVZ and both SMZs) but higher than all WVZ (except for two) and EVZ (85–55°E) glasses. Zr/Hf (Figure 5c) lies at the upper end of the variation evident for the EVZ through W-SMZ and is distinctively higher than in the WVZ. Similar inferences are made for element ratios with a larger spread in incompatibility such as Nb/Zr (Figure 5d), La/Sm (Figure 5e), Sm/Yb (Figure 5f), La/Yb (not shown), and Zr/Y (not shown). These observations indicate low degrees of partial melting and/or melting of variably enriched sources and mixing/pooling of melts generated thereof.

In summary, key element ratios of Ba/Nb, Nb/La, and Zr/Hf of the GRD sample are distinct from WVZ and overlap with the enriched end of EVZ lavas west of 40°E and those of the SMZs. Remarkably, the aforementioned ratios are always higher than those found in the nearest EVZ sampling location at 85°E, which suggests melting of a trace element-enriched source beneath the GRD.

3.3. Radiogenic Isotopes

Radiogenic isotope ratios of Sr-Nd-Pb are not fractionated by magmatic processes and thus can help to more directly characterize the source(s) contributing to melt composition. Published Sr-Nd-Pb isotope data for the Gakkel Ridge (Goldstein et al., 2008) and the Lena Trough (Figure 1d; Nauret et al., 2011) used fresh glass chips and thereby avoided alteration effects that can apply to whole-rock analysis. Namely, exchange with

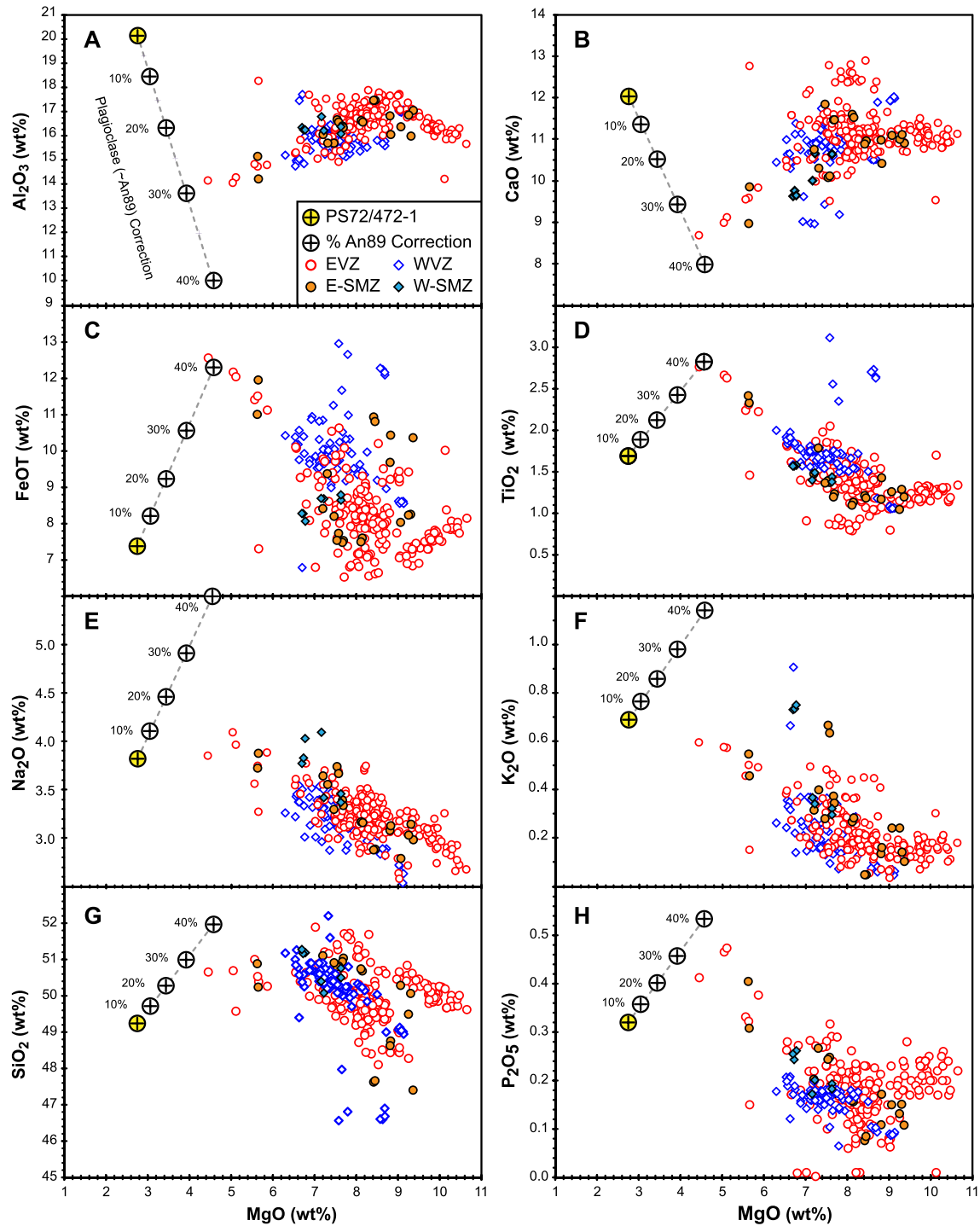


Figure 3. (a–h) Variations of major and minor elements versus MgO as an index of melt differentiation. Bulk rock analysis of PS72/472-1 displays the lowest MgO of all Gakkel samples (data sources same as in Figure 2). The general decrease of Ca and Al with decreasing MgO in the Gakkel samples points to olivine, plagioclase, and clinopyroxene as the principal fractionating mineral phases in the magma reservoirs, and the scatter clearly testifies that the lavas do not originate from a single liquid line of descent. The extreme offset to higher Al and Ca of PS72/472-1 from the Gakkel array indicates accumulation of plagioclase and is consistent with the highly plagioclase phyric nature of this pillow lava. Due to the absence of fresh glass in PS72/472-1, the composition of the erupted melt is simulated by subtraction of An89 plagioclase. See text for more details.

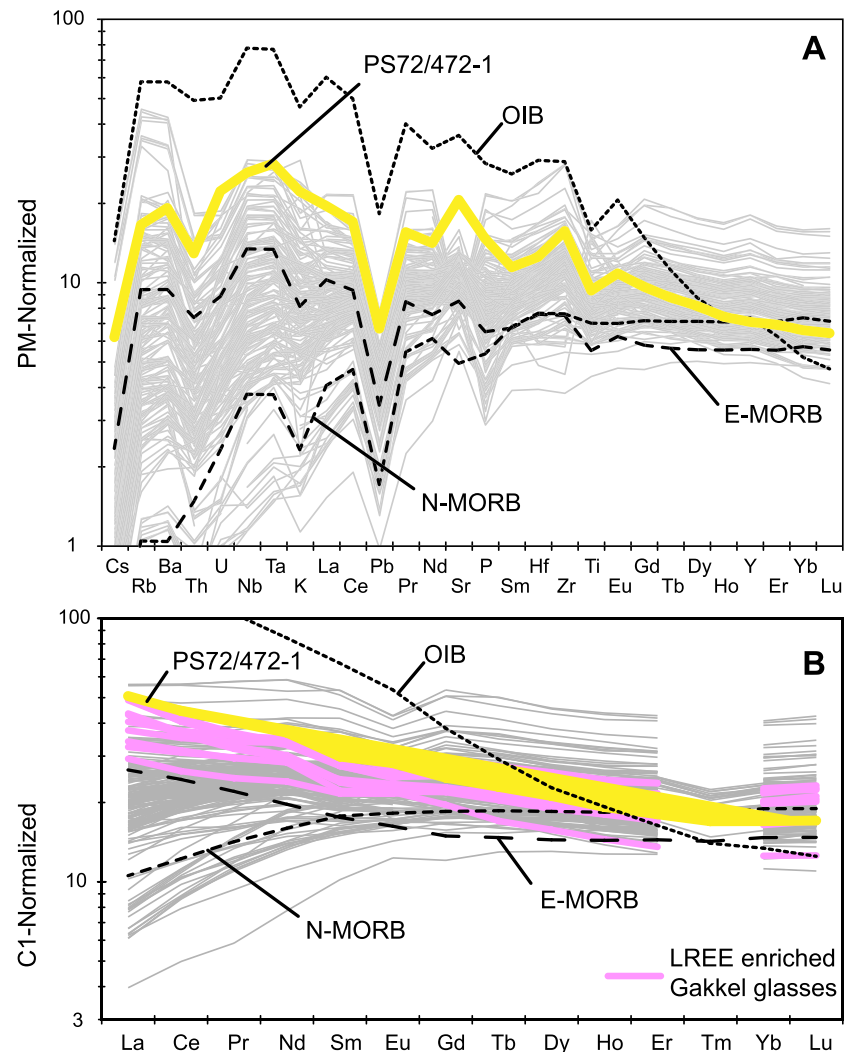


Figure 4. (a) Incompatible element patterns normalized to primitive mantle (Hofmann, 1988). normal MORB, enriched MORB, and Ocean Island Basalt (OIB) from Sun and McDonough (1989) are shown for reference along with glass data from Gakkel Ridge (compilation of Gale et al., 2013, and references therein). The absence of Cs, Rb, Ba, and U peaks in the pattern of PS72/472-1 suggests that seawater alteration is insignificant in this rock and that these fluid-mobile elements can be used to derive petrological information. The GRD sample shows an approximately eightfold enrichment of highly incompatible elements (Cs through Ta) over N-MORB, demonstrating that the lava cannot be derived via melt differentiation from N-MORB. PS72/472-1 appears twofold enriched over reference E-MORB and runs subparallel from Cs through Eu before convergence towards the heavy rare earth elements (HREEs). Gakkel melts display a large variability in incompatible element abundances ranging from sub-N-MORB to E-MORB and beyond. Notably, PS72/472-1 lies at the upper end of the Gakkel field (data sources as in Figure 2) for the highly and moderately incompatible elements and crosses the Gakkel field toward the least incompatible elements. (b) Chondrite-normalized rare earth elements (REEs) after McDonough and Sun (1995) showing PS72/472-1 and Gakkel samples along with reference N-MORB, E-MORB, and OIB (data sources same as in (a)). PS72/472-1 is one of the few Gakkel lavas (10 out of 200) with an enrichment of the light REE over the HREE. Except for one sample the GRD lava uniquely crosses the other LREE-enriched Gakkel patterns toward the HREE.

radiogenic seawater Sr ($^{87}\text{Sr}/^{86}\text{Sr} = \sim 0.7092$ at present and ~ 7 ppm Sr), addition of Rb and U to the rock causing elevated ^{87}Sr and ^{206}Pb ingrowth over longer geological timescales, and mobilization of Pb under hydrothermal conditions (e.g., Jacques et al., 2019). The absence of Rb and U peaks in the multielement pattern of PS72/472-1 already hints at a fairly fresh sample. Moreover, Rb/Sr (0.024) is indistinguishable from the Gakkel glass average (0.026 ± 0.044 2SD, $n = 190$). Nb/U = 36.8 matches the lower end of the canonical Nb/U = 47 ± 10 for mid-ocean ridge basalt (MORB) and OIB (Hofmann et al., 1986) and lies well within the range observed of published Gakkel glasses (Nb/U = 45.5 ± 14.9 2SD, $n = 198$). Similarly,

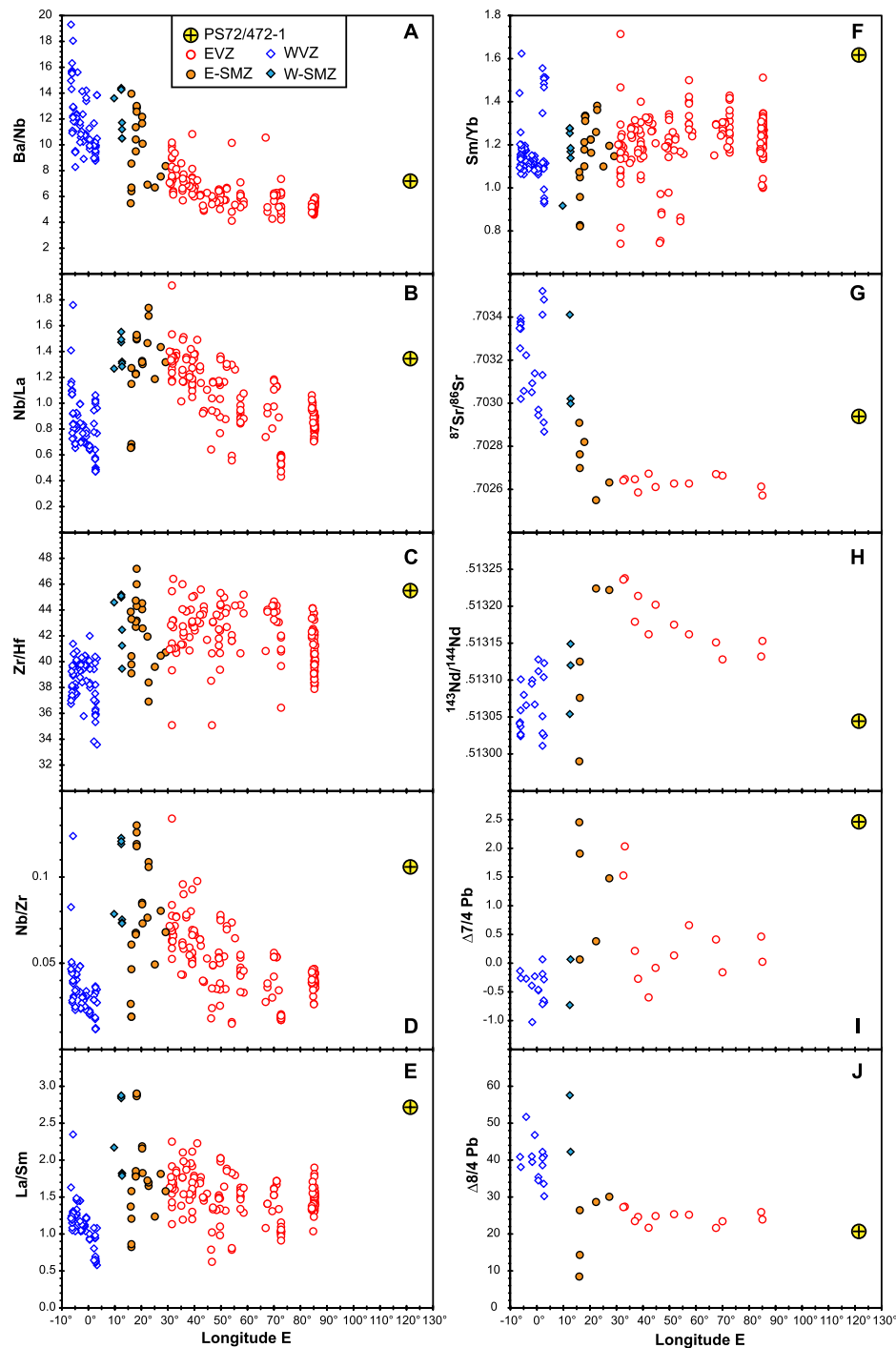


Figure 5. Along-axis variations of incompatible element ratios of (a) Ba/Nb, (b) Nb/La, (c) Zr/Hf, (d) Nb/Zr, (e) La/Sm, and (f) Sm/Yb in Gakkel lavas (data sources as in Figure 2) and PS72/472-1 trace differences and similarities in mantle source characteristics beneath the various segments of the Gakkel ridge (WVZ, SMZs, and EVZ; see Figure 1 for the definitions). Ba/Nb has been previously shown (Goldstein et al., 2008; Michael et al., 2003) to be consistently higher in WVZ and W-SMZ than in EVZ, while that in E-SMZ appears transitional. PS72/472-1 has elevated (a) Ba/Nb, (b) Nb/La, and (c) Zr/Hf compared to the closest EVZ lavas and overlaps with EVZ west of 50°E and some E-SMZ compositions. For element pairs with a larger spread in incompatibility such as (d) Nb/Zr, (e) La/Sm, and (f) Sm/Yb, sample PS72/472-1 belongs to an infrequent group of similarly enriched samples that are present in all Gakkel segments. Most consistent overlap occurs for E-SMZ and W-SMZ except for the lack of similarly high Sm/Yb in E-SMZ lavas. Along-axis variations of (g) $^{87}\text{Sr}/^{86}\text{Sr}$, (h) $^{143}\text{Nd}/^{144}\text{Nd}$, and Pb isotopes expressed as (i) 7/4Pb and (j) 8/4. Other isotope data are from Goldstein et al. (2008) and Nauret et al. (2011). $^{87}\text{Sr}/^{86}\text{Sr}$ of PS72/472-1 is higher than that of the EVZ, lies at the low end of the WVZ array, and is matched by some E-SMZ lavas. $^{143}\text{Nd}/^{144}\text{Nd}$ of the GRD lava is lower than that found in the EVZ and overlaps with the ranges found in both SMZs and WVZ. The high 7/4Pb of PS72/472-1 is solely matched by some E-SMZ and EVZ at 30°E, whereas 8/4Pb groups with EVZ and E-SMZ consistent with 8/4Pb = 30, marking an isotopic boundary at ~14°E (Goldstein et al., 2008).

Ce/Pb = 23.3 lies well within the MORB–OIB range (25 ± 5 ; Hofmann et al., 1986), while all Gakkel glasses have an average Ce/Pb = 22.4 ± 5.7 $2SD$, $n = 192$). Based on these observations, isotope analysis using whole rock of PS72/472-1 is considered to compare equally well to other data (Goldstein et al., 2008; Nauret et al., 2011) obtained on glass. Finally, identical $^{87}\text{Sr}/^{86}\text{Sr} = 0.702942 \pm 5$ ($2SE$) for the leached chips and $^{87}\text{Sr}/^{86}\text{Sr} = 0.702939 \pm 5$ ($2SE$) for leached powders further confirm that both leaching procedures removed any Sr seawater (if present at all) equally well and that $^{87}\text{Sr}/^{86}\text{Sr}$ of this rock can be considered to reflect a pristine magmatic signature.

Along-axis comparison of the Sr–Nd–Pb isotope composition of PS72/472-1 with the published Gakkel data set (Figure 5) shows that the GRD sample has more radiogenic $^{87}\text{Sr}/^{86}\text{Sr}$ than EVZ and most E–SMZ samples and that it straddles at the lower $^{87}\text{Sr}/^{86}\text{Sr}$ range of the WVZ (Figure 5g). $^{143}\text{Nd}/^{144}\text{Nd}$ of PS72/472-1 is less radiogenic than all EVZ and also less radiogenic than many SMZ and WVZ lavas (Figure 5h). Pb isotopes expressed as 7/4Pb and 8/4Pb, denoting the vertical distance from the Northern Hemisphere Reference Line (Hart, 1984) at a given $^{206}\text{Pb}/^{204}\text{Pb}$, show that the GRD sample has significantly higher 7/4Pb (= +2.5) than that of the majority of Gakkel Ridge lavas (7/4Pb = -1.0 to $+0.7$), but falls in the range of EVZ lavas at 33°E and certain E–SMZ (7/4Pb = $+1.5$ to $+2.5$; Figure 5i). In terms of 8/4Pb, PS72/471-1 is similar to values of the EVZ and some E–SMZ (Figure 5j). In summary, the Sr–Nd isotopic compositions of PS72/471-1 are consistently more enriched than those found along the EVZ but overlap with SMZ and WVZ lavas. Notably, the high 7/4Pb of PS72/471-1 is similar to selected E–SMZ and the westernmost EVZ lavas, while 8/4Pb is alike to EVZ and some E–SMZ lavas. At first glance, the ambiguity of Sr–Nd–Pb isotope signals compared to other Gakkel segments indicates that the GRD sample may have a somewhat unique isotopic flavor among the Gakkel lavas. The closest match seems with the Sr–Nd–Pb isotope ratios displayed by selected E–SMZ and two westernmost EVZ lavas. These all have concordantly high 7/4Pb that is absent in all other Gakkel lavas.

3.4. ^{40}Ar – ^{39}Ar Age Dating

To provide a first reliable date for spreading rates at the easternmost end of the Gakkel Ridge, a state-of-the-art age dating was performed. $^{40}\text{Ar}/^{39}\text{Ar}$ incremental heating ages on acid-leached groundmass separates of sample PS72/472-1 are summarized in Table 2 and show that this basalt erupted 3.65 ± 0.01 Ma (2σ). Full $^{40}\text{Ar}/^{39}\text{Ar}$ results, plateau ages, and K/Ca spectra are available as supporting information. We estimate that the 3.7 Ma seamount sample is located approximately 13 km from the axis of spreading, as defined by the projection of the axis of the trough. This implies a full spreading rate of ~ 7 mm/year.

4. Discussion

4.1. Inferences on Depth and Degree of Mantle Melting at the Gakkel Ridge Deep

The large variations of REE ratios such as La/Sm, Sm/Yb, and La/Yb in glasses (compilation of Gale et al., 2013) and melt inclusions (Shaw et al., 2010; Wanless et al., 2014) throughout the Gakkel Ridge cannot result from variable degrees of partial melting of a single, homogeneous source, especially when considering the high variability of these ratios on a local, presumably zero age scale (Figure 5). Possible exception are the more limited variations at 85°E and 72°E of the EVZ (Wanless et al., 2014). Combined with systematic spatial variations of highly incompatible element ratios and radiogenic Sr–Nd–Pb isotope signatures (Figure 5), it is now well established that the mantle beneath the Gakkel Ridge is heterogeneous on local and regional scales, causing the composition of Gakkel melts to reflect a complex interplay of discrete melts from variably enriched sources and their eventual mixing and pooling within the melt column and magma reservoirs (Wanless et al., 2014, and references therein). These authors have carried out a highly detailed study of melt inclusions in olivine and associated volcanic glass at discrete EVZ centers (72°E, 57°E, 39°E, and 31°E, and including the 85°E data from Shaw et al., 2010) that allows them to model melting systematics at high resolution. Their model involves one- and two-component systems with permutations of four parent components that include depleted MORB mantle (DMM), previously DMM, pyroxenite veins, and metasomatized DMM. The best fit model that derives the measured geochemistry is achieved by melting a mix of DMM and metasomatized mantle. Moreover, their modeling indicates an overall decrease in the degree of partial melt from 9–15% at 31°E to 1–6% at 85°E, which correlates positively with the slight decrease of the predicted full spreading rate from 11.09 to 9.93 mm/year (compilation of Gale et al., 2013). Finally, Wanless et al. (2014) also model the average depth of melting in the EVZ mainly in the spinel stability field (approximately 80- to

Table 2
⁴⁰Ar/³⁹Ar Groundmass Incremental Heating Experiments for Gakkel Ridge Sample PS72/472-1.

| Sample information | | | Plateau | | | | Normal isochron | | | | Inverse isochron | | | | Total fusion | | | |
|--------------------|--------------|----------------|----------------------|-------|------|----|-----------------|----------------|-----------|-------|------------------------------------|-----------|-------|------|----------------|-------|--|--|
| Experiment | Sample | Age ±2σ (i) | ³⁹ Ar (%) | K/Ca | MSWD | n | N | Age ±2σ (i) | intercept | ±2σ | ⁴⁰ Ar/ ³⁶ Ar | intercept | ±2σ | MSWD | Age ±2σ (i) | K/Ca | | |
| 17D20242 | PS72-472-1 a | 3.66 ± 0.01 Ma | 68 | 0.184 | 1.04 | 12 | 24 | 3.66 ± 0.02 Ma | 299.66 | ±4.56 | 1.59 | 299.54 | ±4.62 | 1.61 | 3.63 ± 0.01 Ma | 0.197 | | |
| 17D30201 | PS72-472-1 c | 3.65 ± 0.01 Ma | 100 | 0.07 | 0.94 | 24 | 24 | 3.65 ± 0.02 Ma | 294.92 | ±2.80 | 1 | 295.25 | ±2.81 | 0.98 | 3.65 ± 0.01 Ma | 0.13 | | |

Note. a and c denote subsamples from different parts of the PS72-472-1 pillow basalt. 200–180 μm; 1 N HCl (60 min); 6 N HCl (60 min); 1 N HNO₃ (60 min); 3 N HNO₃ (60 min); Mill-Q (60 min).

40-km mantle depth for spinel peridotite) with minor (3%) melt contributions in the garnet stability field (>80 km for garnet peridotite) at 31°E, 39°E, and 72°E. Such detailed evaluations are, however, not possible for the GRD based on a single sample of differentiated lava and lack of a representative regional sampling of the magmatic basement. Nevertheless, the alkalinity of the sample basically implies low degrees of partial melting and/or tapping of an enriched source. But the modeled 1–6% partial melting of clean DMM at 85°E (Wanless et al., 2014) cannot generate the element enrichment observed in PS72/472-1 and thus requires melting of an incompatible element-enriched source at the GRD. Inversely, the predicted and confirmed full spreading rate at the GRD is approximately 6–7 mm/year, which could ultimately lead to even lower degrees of partial melting predicted by extrapolating the 1–6% DMM melting at 85°E (Wanless et al., 2014). At lower spreading rates the thickness of the lithosphere is expected to be thicker and, thus, to truncate the top of the melt column at greater depth and consequently lower the extents of mantle melting (Reid & Jackson, 1981). In summary, even at the lowest possible degree of melting, DMM melting cannot yield the enriched geochemistry of PS72/472-1, thus requiring melting of a geochemically enriched source at the GRD.

4.2. Implications of Mantle Source Signals Along the Gakkel Ridge and GRD

Based on Sr-Nd-Pb isotope (and trace element) ratios, Goldstein et al. (2008) show that the SMZ houses an abrupt mantle compositional boundary around 14°E (Figure 5). Basalts to the west of it (WVZ) feature DUPAL-like (Hart, 1984) source characteristics attributed to shallow recycling of delaminated subcontinental lithospheric mantle during the opening of the Arctic Basin (Goldstein et al., 2008). Counterintuitively, basalts to the east (EVZ) are closest to the Eurasian continent, and generated at the slowest spreading rates, they display isotopic affinities to depleted upper oceanic mantle (DMM), the common source of MORB with incompatible element ratios close to E-MORB. The Sr-Nd-Pb isotopic composition of PS72/472-1 consistently plots with three isotopically enriched samples of the E-SMZ and two of the EVZ in Pb space and lies within or close to the combined field of EVZ and E-SMZ in multi-isotope space (Figures 6a–6c). These relations imply that volcanism at the GRD taps a roughly similar isotopic source as for volcanism in the E-SMZ. Ratios of elements with similar incompatibility such as Ba/Nb, Nb/La, and Zr/Hf versus Sr-Pb isotope ratios (Figures 7a–7i) confirm a compositional association between PS72/472-1 and E-SMZ and EVZ lavas with respect to ⁸⁷Sr/⁸⁶Sr and 8/4Pb, but for ¹⁴³Nd/¹⁴⁴Nd this relation is ambiguous. For element pairs with a larger spread in incompatibility such as Nb/Zr, La/Sm, and Sm/Yb (Figures 7i–7r) the GRD sample plots above the combined E-SMZ–EVZ field. These offsets suggest that the GRD source despite being isotopically similar to some E-SMZ and EVZ lavas has elevated Nb/Zr, La/Sm, and Sm/Yb. Since the number of samples with fully characterized element and isotope data is limited (~40 with Sr-Nd-Pb isotope data versus ~200 with major and trace element data), the discrepancy could reflect analytical bias and/or relate to variable portions of source heterogeneities contributing to the melt process.

The large variations in trace element ratios in E-SMZ and EVZ west of 55°E (Figure 5) indicates melting of a heterogeneous mantle (Wanless et al., 2014, and references therein). According to Wanless et al. (2014), EVZ volcanism is best explained by melting of DMM mixed with metasomatized mantle together with a spatially systematic increase in metasomatized mantle in the EVZ source from 10% at 57°E to a 60% peak in the E-SMZ at 31°E. These findings imply that the volume of metasomatized mantle is not homogeneously distributed within the upper mantle beneath the Gakkel Ridge and can be even absent as suggested for the 72°E and 85°E centers (Wanless et al., 2014). In these areas the degree of melting is modeled, respectively, at 3–9% and 1–6% of a homogeneous DMM source. Importantly, the presence of any, more fusible metasomatized mantle leads to a mismatch between the modeled and observed chemistry of erupted glasses and melt inclusions in olivine (Wanless et al., 2014).

The GRD is located more than 650 km from the nearest sampled site of volcanism at 85°E, where mantle melting exclusively taps DMM (Wanless et al., 2014), and 900 km from the nearest sampling of metasomatized mantle at 57°E. Correlations of La/Sm as an indicator of enrichment versus Ba/Nb and Rb/Nb as an approximation of source-specific finger prints (Figures 8a and 8b) show that PS72/471-1 lies at the extension of the EVZ array and below E-SMZ samples with similarly elevated La/Sm. Notably, PS72/471-1 lies close to the composition of the metasomatized source (Laubier et al., 2012) used by Wanless et al. (2014). These observations confirm that the GRD probes an enriched, most likely metasomatized portion of EVZ (–E-SMZ)-type mantle.

There are several potential explanations for the presence of such a mantle source almost 900 km from the nearest demonstrated occurrence of this material. In the absence of basement sampling between 85°E and the GRD at 121°E, no inference can be made about whether the volume of metasomatized mantle gradually increases eastward in a similar, spatially systematic fashion as is the case in the EVZ to E-SMZ or if such material occurs as irregularly sized domains along the easternmost Gakkel Ridge. The ultraslow spreading at the GRD (6–7 mm/year) limits passive mantle upwelling. Along regular mantle adiabats only the most fusible material is then likely to melt under such conditions, leading to extraction of the purest possible melt from metasomatized mantle, because DMM will not melt, or if it did, only to a very limited extent. This idea is consistent with the more elevated Nb/Zr, La/Sm, and Sm/Yb in the GRD lava compared to the E-SMZ where the DMM contribution is modeled to 40%. In summary, GRD volcanism appears to be fed from a metasomatized mantle similar to mantle found in the E-SMZ and the western part of the EVZ. The ultraslow spreading at the GRD drives mantle upwelling to such low rates that only the most fusible material melts.

The distribution pattern of metasomatized mantle beneath the easternmost Gakkel Ridge can only be resolved by further sampling. Similarly, the melting systematics beneath the GRD can only be more fully understood if samples cover a larger compositional and age range. So far, PS72/472-1 provides only a glimpse into an alkaline melting event 3.65 Ma. Whether this was a single event, pulsating or even continuous, and whether other GRD melts include contributions from DMM must remain unresolved without further sampling.

4.3. Formation and Causes of the GRD

The infrequent volcanism of the SMZ is likely to reflect relatively low degrees of mantle melting in localized zones that are prone to less frequent sampling of compositionally more extreme part of a heterogeneous mantle source region. In this regard, it is interesting that Cochran (2008) note that magmas erupted between the SMZ and EVZ magmatic centers appear to have ascended along faults.

Assuming that the GRD is bounded to the north and south by volcanic centers/ridges, the long-lived nature of GRD magmatism (≥ 3.7 Ma) supports the notion that once established, volcanic centers will tend to maintain themselves as low-viscosity conduits for melts to the surface even in this end-member scenario (Cochran et al., 2003; Dick et al., 2003). Magmatism might be focused initially into discrete centers along the easternmost part of Gakkel Ridge and was linked to a source region that has undergone prior geochemical enrichment.

Another characteristic feature of ultraslow spreading ridges are unusual deep earthquakes in the upper mantle (Jokat et al., 2012; Schlindwein et al., 2013; Schlindwein & Schmidt, 2016), which is very rarely observed at slow and faster mid-ocean ridges. In general, the distribution of the earthquakes down to 40 km along the Knipovich and Southwest Indian ridges and likely also the Gakkel Ridge (Schlindwein et al., 2005) indicate that the uppermost mantle between focused magmatic centres/ridges behaves in a brittle manner. In strong contrast, areas with focused magmatism along the investigated ultraslow spreading ridges show only few earthquakes in the warmer, upper mantle.

The unusual deepness of the GRD in conjunction with limited sediment infill is unique in comparison to the adjacent basins, and thus, the formation of the GRD is enigmatic. Two models exist to explain the feature. Piskarev and Elkina (2017) propose that the GRD is a caldera formed by a large-scale, explosive volcanic eruption around 1 million years ago and that this system operated on a similar scale as did “supervolcanoes” such as Yellowstone. This view is not supported by our findings since the alkaline nature of PS72/472-1 points to a low-volume magmatic system rather than to a large silicic magma reservoir typical of a supervolcano. Systematic GRD basement sampling and geochemical characterization of the volcanic material in the reference sedimentary core located about 1,000 km from the Gakkel Ridge (Piskarev & Elkina, 2017) are required to link the GRD with a large-scale, explosive volcanic event. Nevertheless, explosive release of volatiles on the Gakkel Ridge is evident from unconsolidated pyroclastic deposits blanketing the rift valley at 85° E, which seems to be linked to the discharge of CO₂ that accumulated in (possibly deep) crustal melt reservoirs (Pontbriand et al., 2012; Sohn et al., 2008). Thus, the subsequent buildup and explosive discharge of volatile-rich magmatic foams together with the fact that the GRD is rimmed by several volcanoes that acted as a dam might have played a role in keeping the GRD devoid of sediments. Thus, in our model the GRD is a consequence of focused magmatism along transverse basement ridges. In the western part of Gakkel Ridge a

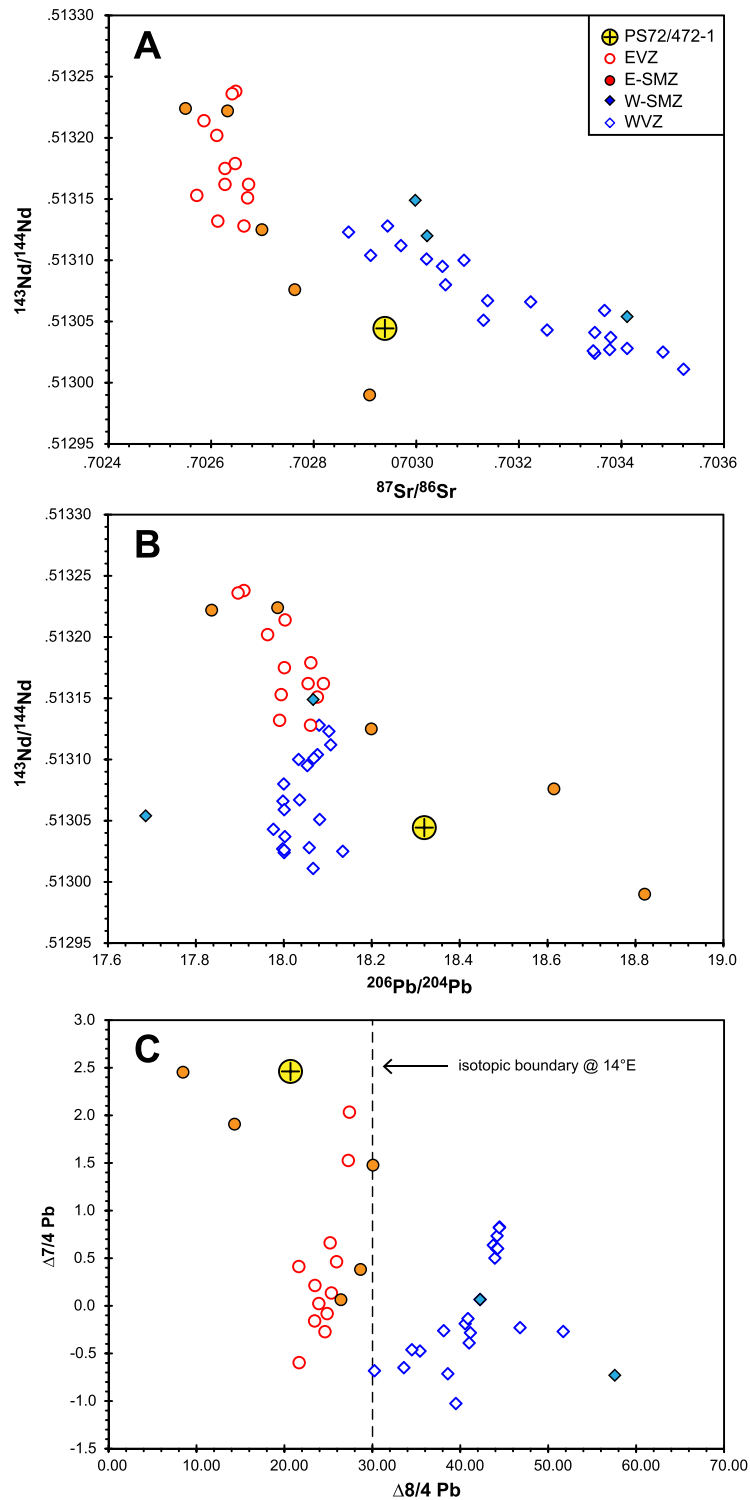


Figure 6. Isotope correlation diagrams of (a) $^{87}\text{Sr}/^{86}\text{Sr}$ versus $^{143}\text{Nd}/^{144}\text{Nd}$, (b) $^{206}\text{Pb}/^{204}\text{Pb}$ versus $^{143}\text{Nd}/^{144}\text{Nd}$, and (c) $8/4\text{Pb}$ versus $7/4\text{Pb}$. The Delta (Δ) notation translates to the vertical deviation from the Northern Hemisphere Reference Line after Hart (1984). Note that the Pb isotope data of Goldstein et al. (2008) and Nauret et al. (2011) are renormalized to the GEOMAR NBS981 values to adjust for small-scale analytical differences between these high-precision data sets. In Sr-Nd isotope space (a), WVZ and EVZ separate reasonably well into distinct arrays. The GRD lava broadly aligns with the steep correlation displayed by the combined EVZ and E-SMZ data and lies below the WVZ Sr-Nd field. Although $^{143}\text{Nd}/^{144}\text{Nd}$ are differential in EVZ and WVZ, they broadly overlap in $^{206}\text{Pb}/^{204}\text{Pb}$ (b). In this respect, the GRD lava aligns vaguely with the broad, correlated field of EVZ and E-SMZ lavas and groups with the few data from E-SMZ. In $7/4\text{Pb}$ versus $8/4\text{Pb}$ space, the GRD lava aligns with a subgroup of similar high- $7/4\text{Pb}$ EVZ and E-SMZ lavas. After Goldstein et al. (2008), $8/4 = 30$ marks a distinct compositional boundary between WVZ + W-SMZ (≥ 30) and EVZ + E-SMZ (≤ 30).

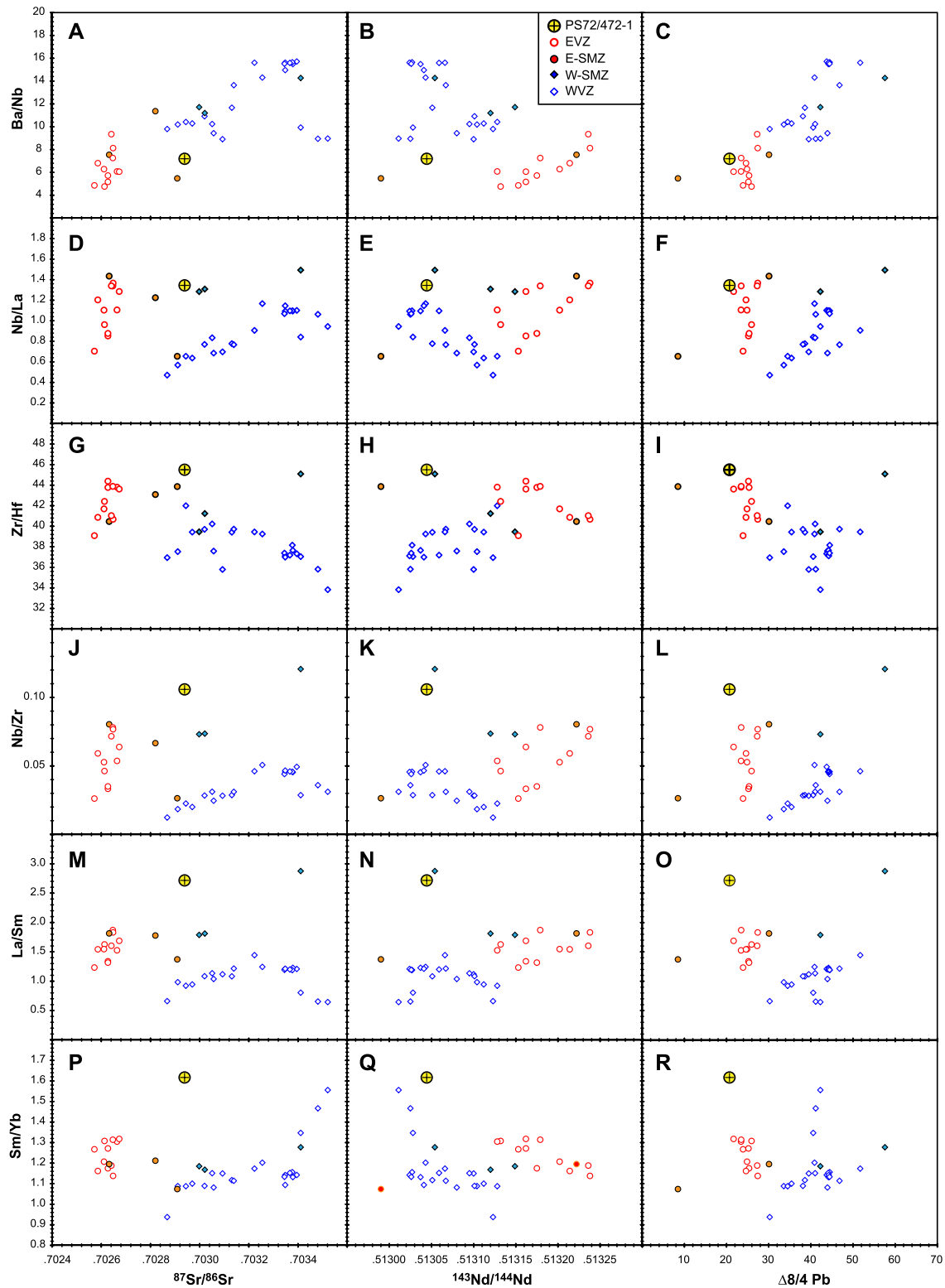


Figure 7. (a–r) Correlation diagrams of $^{87}\text{Sr}/^{86}\text{Sr}$, $^{143}\text{Nd}/^{144}\text{Nd}$ and $8/4\text{Pb}$ versus Ba/Nb, Nb/La, Zr/Hf, Nb/Zr, La/Sm, and Sm/Yb. For element pairs with similar incompatibility (Ba/Nb, Nb/La, and Zr/Hf) the GRD lava aligns with the EVZ–E–SVZ array in $^{87}\text{Sr}/^{86}\text{Sr}$ and $8/4\text{Pb}$ space but falls short for $^{143}\text{Nd}/^{144}\text{Nd}$. For element ratios with a larger spread in incompatibility such as Nb/Zr, La/Sm, and Sm/Yb, PS72/472-1 lies clearly above the EVZ and WVZ arrays. Again, a tentative grouping to the EVZ–E–SMZ field can only be made for $^{87}\text{Sr}/^{86}\text{Sr}$ and $8/4\text{Pb}$. The apparent contradiction to Figure 5 where the enrichment of PS72/472-1 is consistently in agreement with a few W-SMZ and E-SMZ lavas reflects the lack of complementary Sr–Nd–Pb isotope data and/or the GRD lava being dominated by contributions from an enriched source.

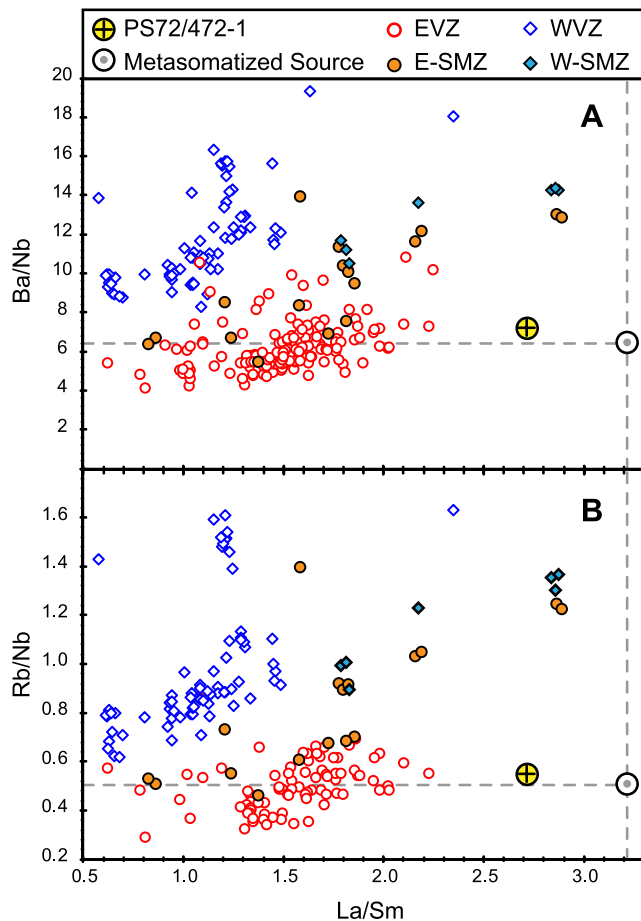


Figure 8. Correlation diagrams of La/Sm versus (a) Ba/Nb and (b) Rb/Nb showing the GRD lava to lie at the extension of EVZ field, suggesting that PS72/472-1 samples an enriched EVZ component that is unsampled in EVZ. At similarly high La/Sm, SVZ lavas display significantly higher Ba/Nb and Rb/Nb than does the GRD lava, indicating that the GRD component is unique in at least these ratios. Notably, PS72/471-1 plots near the metasomatized source of Laubier et al. (2012) (large circle and dashed lines) used by Wanless et al. (2014) to model trace element variability along the EVZ. See text for details.

Acknowledgments

We thank the captain and crew of RV *Polarstern* as well as the geophysical team for their excellent support during cruise ARK-XXVIII/4. We are grateful to Laura Jensen and Boris Dorschel, who provided us with bathymetric maps. These swath bathymetric data are available from Pangaea (<https://doi.pangaea.de/10.1594/PANGAEA.908277>). All data files for the $^{40}\text{Ar}/^{39}\text{Ar}$ dating can be found in the supporting information. We thank Peter Michael, Marcel Regelous, and an anonymous reviewer for their comments, which greatly enhanced the paper.

models. The presented petrological/geophysical data strongly suggest that focused magmatism remains the controlling process for seafloor spreading even at the extreme end of ultraslow spreading rates. The age dating of a single rock sample confirms an ultraslow full spreading rate of ~ 7 mm/year as suggested from aeromagnetic and global GPS data.

References

- Brozna, J. M., Childers, V. A., Lawver, L. A., Gahagan, L. M., Forsberg, R., Faleide, J. I., & Eldholm, O. (2003). New aerogeophysical study of the Eurasia Basin and Lomonosov Ridge: Implications for basin development. *Geology*, *31*, 825–828.
- Cochran, J. R. (2008). Seamount volcanism along the Gakkel Ridge, Arctic Ocean. *Geophysics Journal International*, *174*, 1153–1173. <https://doi.org/10.1111/j.1365-246X.2008.03860.x>
- Cochran, J. R., Kurras, G. J., Edwards, H., & Coakley, B. J. (2003). The Gakkel Ridge: Bathymetry, gravity anomalies, and crustal accretion at extremely slow spreading rates. *Journal of Geophysical Research*, *108*(B2), 2116. <https://doi.org/10.1029/2002JB001830>
- DeMets, C., Gordon, R. G., Argus, D. F., & Stein, S. (1994). Effect of recent revisions to the geomagnetic reversal time scale on estimates of the current plate motions. *Geophysical Research Letters*, *21*(20), 2191–2194.
- Dick, H. J. B., Lin, J., & Schouten, H. (2003). An ultraslow-spreading class of ocean ridge. *Nature*, *426*(6965), 405–412. <https://doi.org/10.1038/nature02128>
- Gale, A., Dalton, C. A., Langmuir, C. H., Su, Y., & Schilling, J.-G. (2013). The mean composition of ocean ridge basalts. *Geochemistry, Geophysics, Geosystems*, *14*, 489–518. <https://doi.org/10.1029/2012GC004334>

total of six volcanic transverse ridges (Figure 1d, blue dashed lines) are observed, which indicate the locations of focused magmatism. Such ridges are difficult to identify in the eastern part, since they are almost covered by thick sediments. The most recent bathymetric data, however, show indications that such ridges also exist between the EVZ and the GRD. We speculate that at least four more volcanic ridges (Figure 1d, dashed yellow lines) exist, and the GRD is part of this segmentation. Finally, while our conclusions cast no doubt on the principal findings of Piskarev and Elkina (2017), we suggest that the source area for the unusual sediment composition in their reference core was located somewhere in the Arctic, but not in the vicinity of the GRD.

Estimations of spreading rates along ultraslow spreading ridges are difficult, since a magnetic anomaly might contain several different magnetic reversals. They cannot be discriminated by shipborne or aeromagnetic surveys because of the large distance of several kilometers between the magnetic source and the sensors. The first published spreading rates from Karasik (1968) and Vogt et al. (1979) had since then a profound influence on the tectonic interpretation of the Gakkel Ridge. Global studies of plate movements (NUVEL-1A; DeMets et al., 1994) also suggested that the full Gakkel Ridge spreading rate decreases from 13 mm/year along the western part of the ridge to 6 mm/year close to the Laptev Sea (Jokat & Schmidt-Aursch, 2007; Karasik, 1968; Vogt et al., 1979). Since then, no rock age dating from the Gakkel Ridge rift valley was available to confirm or withdraw their interpretation. Our $^{40}\text{Ar}/^{39}\text{Ar}$ age of the rock sample from the GRD is in excellent agreement with these studies. Our calculated full spreading rate of 7 mm/year is the first direct age dating confirming the presence of extreme ultraslow spreading rates close to the Laptev Sea.

5. Conclusions

Our observations suggest that the almost sediment-free GRD is the result of interplay between the active Gakkel rift zone, mantle heterogeneities, focused magmatism, rimming volcanoes, and possibly the episodic removal of sediment cover by a volatile buildup and release. The deep rift valley bounded to the north and south by large volcanoes/ridges (?) and distinct mantle source geochemistry allow us to interpret the GRD as the easternmost SMZ. If true, this would indicate that the geometry and geochemistry of the SMZ represent the end-member of seafloor spreading

- Garbe-Schönberg, C.-D. (1993). Simultaneous determination of thirty-seven trace elements in twenty-eight international rock standards by ICP-MS. *Geostandard Newsletter*, 17, 81–97.
- Goldstein, S. L., Soffer, G., Langmuir, C. H., Lehnert, K. A., Graham, D. W., & Michael, P. J. (2008). Origin of a 'Southern Hemisphere' geochemical signature in the Arctic upper mantle. *Nature*, 453, 89–93. <https://doi.org/10.1038/nature06919>
- Hart, S. R. (1984). A large-scale isotope anomaly in the Southern Hemisphere mantle. *Nature*, 309, 753–757. <https://doi.org/10.1038/309753a0>
- Hoernle, K., Hauff, F., Kokfelt, T. F., Haase, K., Garbe-Schönberg, D., & Werner, R. (2011). On- and off-axis chemical heterogeneities along the South Atlantic Mid-Ocean-Ridge (5–11°S): Shallow or deep recycling of ocean crust and/or intraplate volcanism? *Earth and Planetary Science Letters*, 306(1-2), 86–97. <https://doi.org/10.1016/j.epsl.2011.03.032>
- Hofmann, A. W. (1988). Chemical differentiation of the Earth: The relationship between mantle, continental and oceanic crust. *Earth and Planetary Science Letters*, 90, 297.
- Hofmann, A. W., Jochum, K. P., Seufert, M., & White, W. M. (1986). Nb and Pb in oceanic basalts: New constraints on mantle evolution. *Earth and Planetary Science Letters*, 79, 33–45.
- Jacques, G., Hauff, F., Hoernle, K., Werner, R., Uenzelmann-Neben, G., Garbe-Schönberg, D., & Fischer, M. (2019). Nature and origin of the Mozambique Ridge, SW Indian Ocean. *Chemical Geology*, 507, 9–22. <https://doi.org/10.1016/j.chemgeo.2018.12.027>
- Jakobsson, M., Mayer, L., Coakley, B., Dowdeswell, J. A., Forbes, S., Fridman, B., et al. (2012). The international bathymetric chart of the Arctic Ocean (IBCAO) version 3.0. *Journal of Geophysical Research*, 39, L12609. <https://doi.org/10.1029/2012GL052219>
- Jokat, W. (2009). *The expedition of the research vessel "Polarstern" to the Arctic in 2008 (ARK-XXIII/3), Reports on Polar and Marine Research*. Bremerhaven: Alfred-Wegener-Institut. <http://hdl.handle.net/10013/epic.33317>
- Jokat, W., Kollofrath, J., Geissler, W., & Jensen, L. (2012). Crustal thickness and earthquake distribution south of the Logachev Seamount, Knipovich Ridge. *Geophysical Research Letters*, 39, L08302. <https://doi.org/10.1029/2012GL051199>
- Jokat, W., & Micksch, U. (2004). The sedimentary structure of Nansen and Amundsen basins. *Geophysical Research Letters*, 31, L02603. <https://doi.org/10.1029/2003GL018352>
- Jokat, W., Ritzmann, O., Schmidt-Aursch, M. C., Drachev, S., Gauger, S., & Snow, J. (2003). Geophysical evidence for reduced melt production on the ultraslow Gakkel Ridge (Arctic Ocean). *Nature*, 423(6943), 962–965. <https://doi.org/10.1038/nature01706>
- Jokat, W., & Schmidt-Aursch, M. C. (2007). Geophysical characteristics of the ultraslow spreading Gakkel Ridge, Arctic Ocean. *Geophysics Journal International*, 168, 983–998. <https://doi.org/10.1111/j.1365-246X.2006.03278.x>
- Karasik, A. M. (1968). Magnetic anomalies of the Gakkel Ridge and origin of the Eurasia Subbasin of the Arctic Ocean. *Geophysical Methods Prospect Arctic*, 5, 8–19.
- Klein, E. M., & Langmuir, C. H. (1987). Global correlations of ocean ridge basalt chemistry with axial depth and crustal thickness. *Journal of Geophysical Research*, 92(B8), 8089–8115.
- Konrad, K., Koppers, A. A. P., Steinberger, B., Finlayson, V., Konter, J., & Jackson, M. G. (2018). On the relative motions of long-lived Pacific mantle plumes. *Nature Communications*, 9(1), 1–8. <https://doi.org/10.1038/s41467-018-03277-x>
- Koppers, A. A. P. (2002). ArArCALC – software for ⁴⁰Ar/³⁹Ar age calculations. *Computers Geosciences*, 5, 605–619. [https://doi.org/10.1016/S0098-3004\(01\)00095-4](https://doi.org/10.1016/S0098-3004(01)00095-4)
- Koppers, A. A. P., Yamazaki, T., Geldmacher, J., Gee, J. S., Pressling, N., Koppers, A. A. P., et al. (2012). Limited latitudinal mantle plume motion for the Louisville hotspot. *Nature Geoscience*, 5(12), 911–917. <https://doi.org/10.1038/ngeo1638>
- Kuiper, K. F., Deino, A., Hilgen, F. J., Krijgsman, W., Renne, P. R., & Wijbrans, J. R. (2008). Synchronizing the rock clocks of Earth history. *Science*, 320(5875), 500–504. <https://doi.org/10.1126/science.1154339>
- Laubier, M., Gale, A., & Langmuir, C. H. (2012). Melting and crustal processes at the FAMOUS segment (Mid-Atlantic Ridge): New insights from olivine-hosted melt inclusions from multiple samples. *Journal of Petrology*, 53(4), 665–698.
- Le Maitre, R. W., et al. (2005). *Igneous rocks: A classification and glossary of terms: Recommendations of the International Union of Geological Sciences Subcommission on the Systematics of Igneous Rocks*. 252 S. Cambridge, UK: Cambridge University Press.
- MacDonald, G. A., & Katsura, T. (1964). Chemical composition of Hawaiian lavas. *Journal of Petrology*, 5, 82–133.
- McDonough, W. F., & Sun, S.-S. (1995). The composition of the Earth. *Chemical Geology*, 120, 223–253.
- Michael, P. J., Langmuir, C. H., Dick, H. J. B., Snow, J. E., Goldstein, S. L., Graham, D. W., et al. (2003). Magmatic and amagmatic seafloor generation at the ultraslow-spreading Gakkel Ridge, Arctic Ocean. *Nature*, 423(6943), 956–961. <https://doi.org/10.1038/nature01704>
- Min, K. W., Mundil, R., Renne, P. R., & Ludwig, K. R. (2000). A test for systematic errors in Ar-40/Ar-39 geochronology through comparison with U/Pb analysis of a 1.1-Ga rhyolite. *Geochimica et Cosmochimica Acta*, 64, 63–98. [https://doi.org/10.1016/S0016-7037\(99\)00204-5](https://doi.org/10.1016/S0016-7037(99)00204-5)
- Müller, C., & Jokat, W. (2000). Seismic evidence for volcanic activity at the eastern Gakkel Ridge. *EOS Transactions*, 81(24), 265–269.
- Nauret, F., Snow, J. E., Hellebrand, E., & Weis, D. (2011). Geochemical composition of K-rich lavas from the Lena Trough (Arctic Ocean). *Journal of Petrology*, 52, 1185–1206.
- Nikishin, A. M., Gaina, C., Petrov, E. I., Malyshev, N. A., & Freiman, S. I. (2017). Eurasia Basin and Gakkel Ridge, Arctic Ocean: Crustal asymmetry, ultra-slow spreading and continental rifting revealed by new seismic data. *Tectonophysics*, 746, 64–82. <https://doi.org/10.1016/j.tecto.2017.09.006>
- Piskarev, A., & Elkina, D. (2017). Giant caldera in the Arctic Ocean: Evidence of the catastrophic eruptive event. *Scientific Reports*, 7, 46248. <https://doi.org/10.1038/srep46248>
- Pontbriand, C. W., Soule, S. A., Sohn, R. A., Humphris, S. E., Kunz, C., Singh, H., et al. (2012). Effusive and explosive volcanism on the ultraslow-spreading Gakkel Ridge, 85°E. *Geochemistry Geophysics Geosystems*, 13, Q10005. <https://doi.org/10.1029/2012GC004187>
- Reid, I., & Jackson, H. R. (1981). Oceanic spreading rate and crustal thickness. *Marine Geophysical Research*, 5, 165–172.
- Rohde, J., Hoernle, K., Hauff, F., Werner, R., O'Connor, J., Class, C., et al. (2013). 70 Ma chemical zonation of the Tristan-Gough hotspot track. *Geology*, 41(3), 335–338. <https://doi.org/10.1130/G33790.1>
- Schlindwein, V., Bergner, A., Geissler, W. H., & Jokat, W. (2013). Seismic gap beneath Logachev Seamount: Indicator for melt focussing at an ultraslow mid-ocean ridge? *Geophysical Research Letters*, 40, 1703–1707. <https://doi.org/10.1002/grl.50329>
- Schlindwein, V., Mueller, C., & Jokat, W. (2005). Seismoacoustic evidence for volcanic activity on the ultraslow spreading Gakkel Ridge, Arctic Ocean. *Geophysical Research Letters*, 32, L18306. <https://doi.org/10.1029/2005GL023767>
- Schlindwein, V., & Schmidt, F. (2016). Mid-ocean-ridge seismicity reveals extreme types of ocean lithosphere. *Nature*, 535(7611), 276–279. <https://doi.org/10.1038/nature18277>
- Selektov, S. B. (2002). Structure and tectonic evolution of the Southern Eurasia Basin, Arctic Ocean. *Tectonophysics*, 351, 193–243.

- Shaw, A. M., Behn, M. D., Humphris, S. E., Sohn, R. A., & Gregg, P. M. (2010). Deep pooling of low degree melts and volatile fluxes at the 85°E segment of the Gakkel Ridge: Evidence from olivine-hosted melt inclusions and glasses. *Earth and Planetary Science Letters*, *289*, 311–322.
- Sohn, R. A., Willis, C., Humphris, S., Shank, T. M., Singh, H., Edmonds, H. N., et al. (2008). Explosive volcanism on the ultraslow-spreading Gakkel Ridge, Arctic Ocean. *Nature*, *453*(7199), 1236–1238. <https://doi.org/10.1038/nature07075>
- Sun, S.-S., & McDonough, W. F. (1989). Chemical and isotopic systematics of oceanic basalts: Implications for mantle composition and processes. In A. D. Saunders & M. J. Norry (Eds.), *Magmatism in the ocean basins* (pp. 313–345). London: Blackwell.
- Vogt, P. R., Taylor, P. T., Kovacs, L. C., & Johnson, G. L. (1979). Detailed aeromagnetic investigations of the Arctic Basin. *Journal of Geophysical Research*, *84*, 1071–1089.
- Wanless, V. D., Behn, M. D., Shaw, A. M., & Plank, T. (2014). Variations in melting dynamics and mantle compositions along the Eastern Volcanic Zone of the Gakkel Ridge: Insights from olivine-hosted melt inclusions. *Contributions to Mineralogy and Petrology*, *167*, 1005.